The final publication is available at

https://doi.org/10.1021/acsanm.0c01392

Additional Information

Ultra-Stable Magnetic Nanoparticles Encapsulated in Carbon for Magnetically Induced Catalysis

Luis M. Martínez-Prieto,[1,±] Julien Marbaix,[2,±] Juan M. Asensio,[2] Christian Cerezo-Navarrete,[1] Pier-Francesco Fazzini,[2] Katerina Soulantica,[2] Bruno Chaudret[2,*] and Avelino Corma[1,*]

[1] ITQ, Instituto de Tecnología Química, CSIC-Universitat Politècnica de València, Av. de los Naranjos S/N 46022, Valencia, España

[2] LPCNO, Laboratoire de Physique et Chimie des Nano-Objets, UMR5215 INSA-CNRS UPS, Institut des Sciences appliquées, 135, Avenue de Rangueil, F-31077 Toulouse, France.

[±] These authors contributed equally to this work

E-mails: chaudret@insa-toulouse.fr acorma@itq.upv.es

Keywords: magnetic nanoparticles • carbon encapsulation • magnetic catalysis • methanation • propane dry reforming • propane dehydrogenation
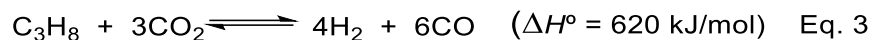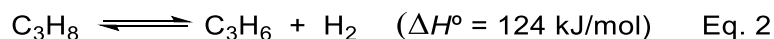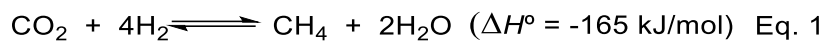
Abstract

Magnetically induced catalysis using magnetic nanoparticles (MagNPs) as heating agents is a new efficient method to perform reactions at high temperatures. However, the main limitation is the lack of stability of the catalysts operating in such harsh conditions. Normally, above 500 ºC, significant sintering of MagNPs takes place. Here we present encapsulated magnetic FeCo and Co

NPs in carbon (**Co@C** and **FeCo@C**) as an ultra-stable heating material suitable for high temperature magnetic catalysis. Indeed, **FeCo@C** or a mixture of **FeCo@C:Co@C (2:1)** decorated with Ni or Pt-Sn showed good stability in terms of temperature and catalytic performances. In addition, consistent conversions and selectivities regarding conventional heating were observed for CO_2 methanation (Sabatier Reaction), propane dehydrogenation (PDH) and propane dry reforming (PDR). Thus, the encapsulation of MagNPs in carbon constitutes a major advance in the development of stable catalysts for high temperature magnetically induced catalysis.

Introduction

Magnetic heating is an attractive alternative to conventional heating that has been gaining attention in catalysis during the last years. Indeed, magnetically induced catalysis using magnetic nanoparticles (MagNPs) has been succesfully applied in solution[1-6] as well as in gas-phase reactions.[7-14] It is based on the principle that ferromagnetic materials can release heat to the environment through hysteresis losses in the presence of an oscillating magnetic field. The main advantage of magnetic heating relies on the very fast warming up of the system, which makes this system adapted to the storage of intermittent energies, as well as on the direct heating of the catalyst without the need for heating the whole reactor.[15] This makes magnetic heating a promising method to perform reactions that occur at medium/high temperatures, such as CO_2 methanation (Sabatier Reaction), propane dehydrogenation (PDH) or propane dry reforming (PDR). The heating power of MagNPs is commonly quantified by the specific absorption rate (*SAR*), which measures the energy released per unit of mass upon magnetic excitation. In particular, when applying an alternating magnetic field with a frequency f and an amplitude $\mu_0 H_{rms}$ to MagNPs, the area of the hysteresis loop is proportional to the dissipated energy.[16]

The current context of global warming has stimulated the development of catalytic reactions that utilize CO_2 as a platform molecule for the production of fuels or chemicals, with the objective of reducing the global carbon footprint. CO_2 hydrogenation (the so-called Sabatier reaction) (Eq. 1) is one of the main synthetic routes to produce methane. Although it is an exothermic reaction, it is usually performed above 250-300 ºC, due to the high kinetic barrier for the activation of the CO_2 molecule,[17-19] and development of catalysts able to work at lower temperature is an important issue.[20] Even if Sabatier reaction is presently exploited at industrial scale, it requires an important energy supply to reach the operating conditions. This is one of the limitations of Power-To-Gas (P2G) technology, where the excess of electricity is used to produce methane.[21] Therefore, energetically efficient processes that can be rapidly started or stopped are of high interest due to the possibility to carry out the hydrocarbon production only when the weather conditions allow it. In this context, magnetic heating can be an interesting alternative for intermittent energy storage or P2G. On the other hand, a catalyst displaying good magnetic heating performances would enable to perform more efficiently endothermic reactions that require high-energy supplies. Since the catalyst itself, and not the reactor, is the heating source, the energy transfer is rapid and efficient. Another reaction of industrial interest is the endothermic dry reforming of propane (PDR), which can be a solution to the increasing demand of synthesis gas (CO, H_2) or the hydrogen production for industrial applications.[22] Similarly, dehydrogenation of light alkanes (e.g. propane) has received great attention because of the growing need of light olefins for the production of chemicals.[23] These reactions occur at high temperatures, above 600°C in the case of propane dehydrogenation (PDH; Eq. 2) and from 550°C to 900°C for propane dry reforming (PDR; Eq. 3).[22,23] Dry reforming is generally catalyzed by Ni-based catalysts,[24] while PDH is catalyzed by Pt-based catalysts reaching excellent selectivities to propene.[25-27]

$$CO_2 + 4H_2 \rightleftharpoons CH_4 + 2H_2O \quad (\Delta H^o = -165 \text{ kJ/mol}) \quad \text{Eq. 1}$$

$$C_3H_8 \rightleftharpoons C_3H_6 + H_2 \quad (\Delta H^o = 124 \text{ kJ/mol}) \quad \text{Eq. 2}$$

$$C_3H_8 + 3CO_2 \rightleftharpoons 4H_2 + 6CO \quad (\Delta H^o = 620 \text{ kJ/mol}) \quad \text{Eq. 3}$$

The Curie temperature (*Tc*) is the temperature at which a ferromagnetic material becomes superparamagnetic, hence losing its magnetic heating capacity. Thus, the composition of the heating agent is of high importance as the *Tc* of the MagNPs defines the highest temperature that can be theoretically attained by magnetic induction. Therefore, a precise control of the *Tc* of the heating agents will determine their further applicability in the magnetically-induced catalysis of various reactions, when associated to appropriate catalytically active phases. In a recent publication, it has been reported that iron and iron carbide NPs are inefficient to activate high temperature catalysis by magnetic heating while FeCo NPs reach temperatures high enough to significantly activate PDR and PDH.[10] However, especially in cases where high temperatures are required, a main limitation of magnetically-induced reactions is the lack of stability of the catalysts that need to be active for long reaction times under harsh conditions. It was observed that, for temperatures above 500°C, massive sintering of both heating and catalytic nanoparticles occurred, together with carbon deposition which led to deactivation of the catalyst.[10] These processes reduce both the catalytic and heating properties of the NPs and therefore the magnetically-induced catalyst lifetime. In this respect, metal nanoparticles (MNPs) encapsulated in carbon have emerged as efficient sinter-resistant materials thanks to their high thermal stability and confinement properties.[28-30]

Herein, we present novel heating agents for magnetically-induced catalysis based on magnetic Co and FeCo nanoparticles encapsulated in carbon (**FeCo@C** and **Co@C**). Encapsulation in carbon not only protects them from full oxidation, as was recently described,[28,29] but it also confers

to the materials the stability necessary to avoid sintering at such high temperatures. **FeCo@C** and **Co@C** were fully characterized by common techniques, such as Transmission Electron Microscopy (TEM), High resolution TEM (HRTEM), Energy-dispersive X-ray spectrometry (EDX), Inductively Coupled Plasma (ICP), RAMAN Spectroscopy, X-Ray Photoelectron Spectroscopy (XPS), X-ray Powder Diffraction (XRD), Temperature-Programmed Reduction (TPR) and Vibrating-Sample Magnetometer (VSM). In this work we demonstrate that **FeCo@C** and **Co@C** (5 % wt) can be used as heating agents in magnetically-induced reactions taking place at temperatures above 600 °C, maintaining their morphology and heating capacity. These ultra-stable materials (**FeCo@C** and **Co@C**) have been decorated with Ni or Pt-Sn and evaluated in methanation, propane dry reforming and dehydrogenation of propane, presenting high stability in all the cases without modification of their catalytic performances.

Results and discussion

1. Synthesis and characterization

The methodology to encapsulate MagNPs in carbon is based on a two-step procedure. FeCo prepared by a previously reported procedure[31,32] and Co nanoparticles prepared by adaptation of the same procedure (see Experimental part, section 2) were supported on activated carbon (FeCo/C and Co/C; 5 wt %). Then, the MagNPs were encapsulated in carbon through a pyrolysis process (600 ºC, 2 h, 10 ºC/min) to afford FeCo and Co NPs covered by a narrow carbon layer (Figure 1; **FeCo@C** and **Co@C**). The detailed synthetic procedure is described in the experimental section (see Experimental part, section 2). The metal contents of **FeCo@C** and **Co@C** were determined by ICP Atomic Emission Spectroscopy (ICP-AES). Specifically, **FeCo@C** (Fe: 2.6 wt% and Co 2.3 wt%, corresponding to a NP composition of $Fe_{54}:Co_{46}$) and **Co@C** (Co: 4.8 wt%) presented metal contents very close to the theoretical ones (5 wt%).
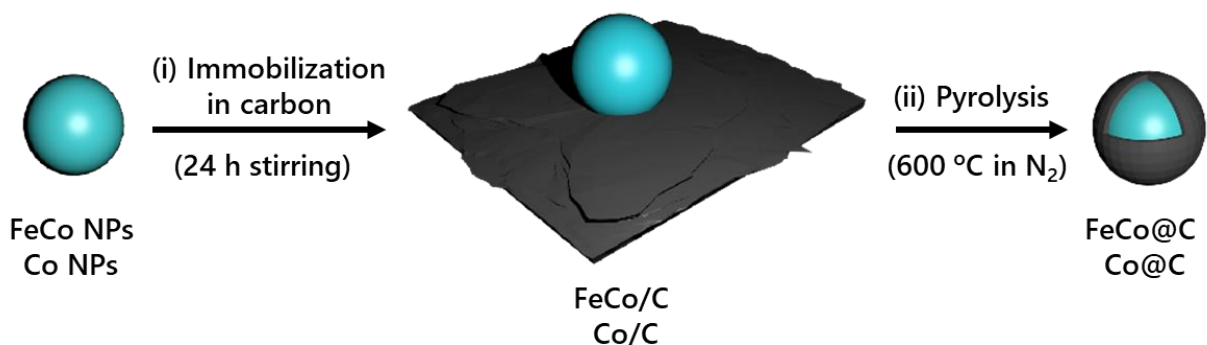
Figure 1. Synthesis of **FeCo@C** and **Co@C** following a two steps synthetic procedure: (i) formation of FeCo/C and Co/C by the immobilization of MagNPs on activated carbon (24 h stirring at room temperature) and (ii) pyrolysis of FeCo/C and Co/C (2h at 600 °C under N_2 flow, 10 °C/min).

TEM analysis of FeCo and Co NPs before encapsulation show spherical and well-distributed nanoparticles, with a good dispersion and a main diameter of *ca.* 10-11 nm (see SI, Figures S1-S3). The size and morphology of **FeCo@C** (10.1 ± 2.0 nm; Figure 2, a-c) and **Co@C** (10.5 ± 1.9 nm; Figure 2, d-f) are very similar to those found in the NPs before encapsulation.
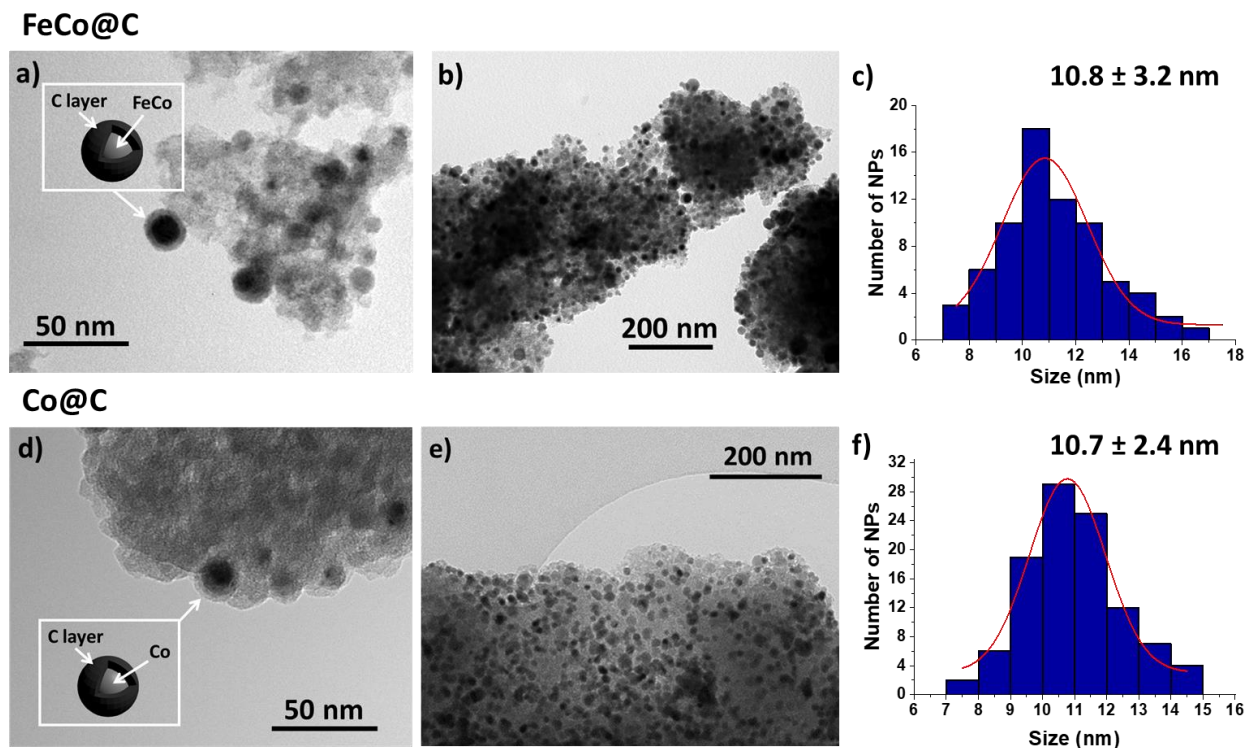
FeCo@C

a)

C layer | FeCo

50 nm

b)

200 nm

c)

10.8 ± 3.2 nm

Co@C

d)

C layer | Co

50 nm

e)

200 nm

f)

10.7 ± 2.4 nm

Figure 2. TEM micrographs and illustrations (insets) of **FeCo@C** (a-b) and **Co@C** (d-e) with their corresponding size histograms [**FeCo@C** (c) and **Co@C** (f)].

The morphology, composition and crystallinity of **FeCo@C** and **Co@C** were studied by High-resolution TEM (HRTEM), Energy-dispersive X-ray spectrometry (EDX) and Scanning transmission electron microscopy (STEM) using a high-angle annular dark-field detector (HAADF). HRTEM micrographs indicate the existence of crystalline NPs encapsulated by a carbon layer with a thickness between 2 and 5 nm (Figures 3a-b and 3d-e). This carbon layer possesses a double function: i) protecting the magnetic FeCo and Co NPs from full oxidation by air, and ii) preventing their sintering under the high temperatures reached under catalytic conditions. However, the carbon layer is not continuous over the whole nanoparticle, since it presents some gaps or cracks (Figures 3b and 3e). The presence of these cracks was corroborated by a simple digestion experiment.[33] More specifically, Co and FeCo NPs encapsulated in carbon were dissolved in a H_2SO_4 solution suggesting that the NPs were not totally covered by carbon

7

(for more details see Experimental part, section 6). The carbon-encapsulated Co nanoparticles (**Co@C**) exhibit an *fcc* cobalt core with a lattice spacing of 2.06 Å that corresponds to (111) plane, and cobalt oxide (CoO_x) regions on their surface with a fringe spacing of 2.42 Å, which belongs to (113) plane (Figure 3c). Similarly, the core of **FeCo@C NPs** presents a *bcc* structure with a lattice spacing of 2.03 Å with some oxide at the surface (Figure 3f). The cracked carbon layer explains the partial oxidation of **Co@C** and **FeCo@C** NP surface after exposure to air. In both systems, the space between the carbon layers is around of 3.6-3.4 Å (Figures 3c and 3f), which corresponds to a turbostratic ordering of the carbon.
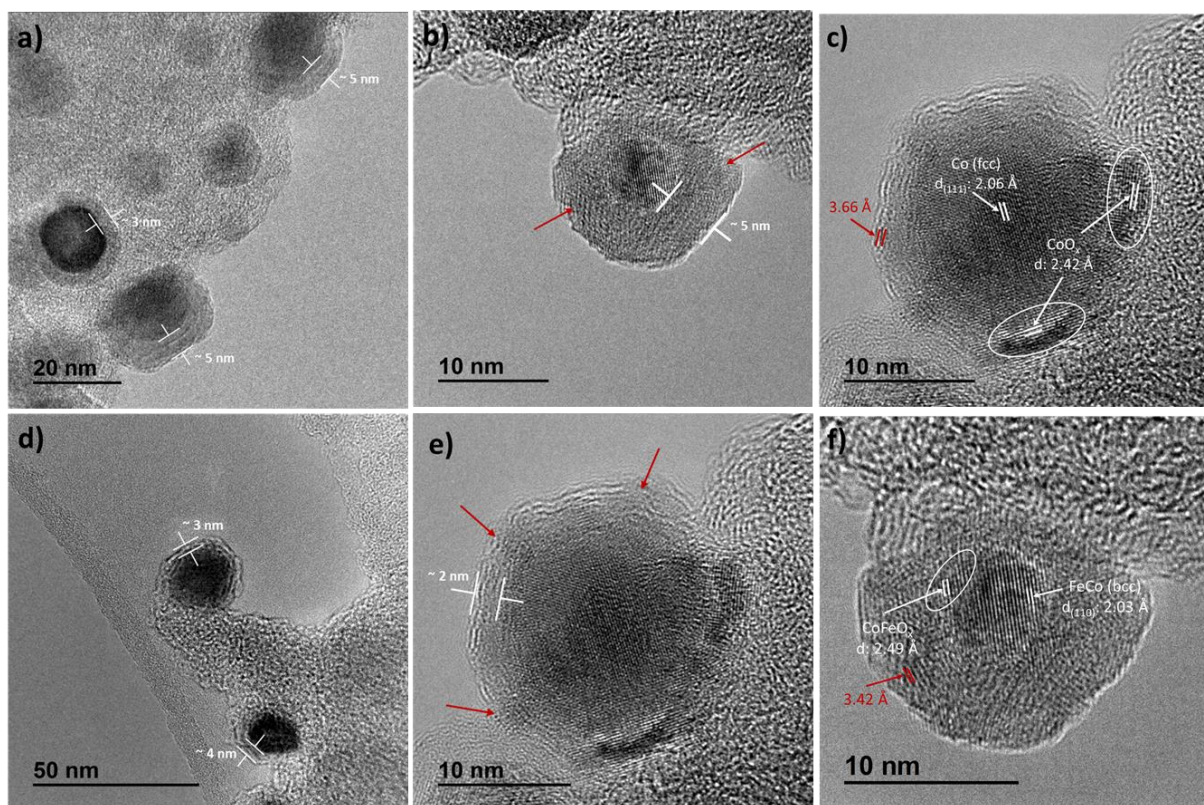

Figure 3. HRTEM micrographs of **Co@C** (a-c) and **FeCo@C** (d-f). The cracks of the carbon layer are highlighted by red arrows (b, e). The lattice spacing of **Co** and **FeCo NPs** are in white and the separation of the carbon layers in red (c, f).

Figures S4 and S5 (see SI) show STEM-HADDF images, and EDX analysis of **Co@C** and **FeCo@C**, respectively. EDX mapping of carbon, cobalt and oxygen elements within **Co@C** (Figure S4a-d) confirms the partial oxidation of the enclosed-Co NPs. Elemental mapping of **FeCo@C** demonstrates the bimetallic nature of these NPs (see SI, Figure S5a-d), with an atomic composition of $Fe_{47}:Co_{53}$ (see SI, Figure S6), which agrees with the theoretical composition ($Fe_{50}:Co_{50}$), and match with the ICP results obtained (*vide supra*). In the EDX composition profiles, we can observe that both MagNPs are embedded either in a thin carbon layer (e.g. 1-2 nm, Figures 3b and 4e) or in a thicker one (e. g. 4-5 nm; Figures 3e 5e).

Figure S7 (See SI) shows X-Ray diffraction (XRD) diffractograms for **Co@C** and **FeCo@C**. Both materials present a (002) peak at $2\theta = 26.4°$ with an interlayer separation of $d = 3.36$ Å, which corresponds to the carbon material. In addition, **Co@C** XRD exhibits *fcc*-Co and CoO_x peaks with relatively low intensities due to the low metal loading (~ 5%). **FeCo@C** XRD also presents some minor peaks, which correspond to *bcc* FeCo and FeCo oxides ($FeCoO_x$). XRD confirms the partial oxidation of the MagNPs encapsulated by the cracked carbon layer when they are exposed to air. These results are in good agreement with HRTEM and EDX observations. Raman spectra of **Co@C** and **FeCo@C** NPs (see SI, Figure S8) display two major bands at 1313-1307 cm^{-1} (D peak) and 1600-1595cm^{-1} (G peak), associated to carbon materials.[34] The high intensity of the D peak is related to the large percentage of disorder present in these carbon materials. The region between 200 and 800 cm^{-1} of **Co@C** spectrum exhibits the typical vibrational modes of Co_3O_4 ($3F_{2g}$, E_g, and A_{1g}) at 194 (F_{2g}), 474 (E_g), 517 (F_{2g}), 619 (F_{2g}) and 691 (A_{1g}) cm^{-1}.[35] **FeCo@C** spectrum also shows the $FeCo_2O_4$ vibrational modes but with a lower intensity and slightly shifted to minor frequencies 189 (F_{2g}), 465 (E_g), and 672 (A_{1g}).[36]

The oxidation state and reducibility of these carbon-encapsulated MagNPs was investigated by X-ray photoelectron spectroscopy (XPS) and temperature-programmed reduction (TPR). By TPR we found that the reduction temperatures for **Co@C** and **FeCo@C** were 320 ºC and 351 ºC, respectively (see SI, Figures S9). Figure S10 (see SI) shows the Co2p area of **Co@C** before and after reduction by H_2 at 400 ºC. The as-synthesized **Co@C** spectrum presents a main peak at 780.7 eV that can attributed to CoO_x species. After reaction at 400 ºC under H_2 atmosphere during 4 h, the CoO_x surface was totally reduced to Co^0 since the spectrum only exhibits a single signal at 778.4 eV, characteristic of metallic cobalt.[37] A similar behavior was observed for **FeCo@C** (see SI, Figure S11), where we can see a clear reduction of Fe and Co in Fe2p and Co2p regions, respectively. These results confirm that the surface of the as-synthesized samples is fully oxidized but that it can be reduced under reductive conditions, which might increase the magnetic heating capacity of the materials under operating catalytic conditions.

The magnetic properties of **Co@C** and **FeCo@C** have been measured by Vibrating Sample Magnetometry (VSM). Saturation magnetization (M_s) and coercive field ($\mu_0 H_c$) have been determined from the hysteresis cycles (Figure 4). For both samples, M_s is close to 120 $A \cdot m^2 \cdot g^{-1}$ at 300 K and 130 $A \cdot m^2 \cdot g^{-1}$ at 5 K. These values are below those reported for the bulk materials, (230 $A \cdot m^2 \cdot g^{-1}$ for bulk FeCo and 165 $A \cdot m^2 \cdot g^{-1}$ for Co),[38] This reduction can be due to both surface oxidation and incorporation of carbon into the Co and FeCo lattice during the encapsulation of the NPs into carbon. Indeed, the formation of cobalt carbide[39] or the incorporation of carbon into FeCo NPs[40-41] is known to lead to species showing a depleted Ms. Partial oxidation was confirmed by the presence of a small *exchange bias* observed in the hysteresis loops at 5 K after a field-cooling in the presence of a $\mu_0 H$ of 3 T, which is characteristic of the coupling between ferromagnetic and

antiferromagnetic layers.[42] However, it is presumably not sufficient to explain the strong depletion

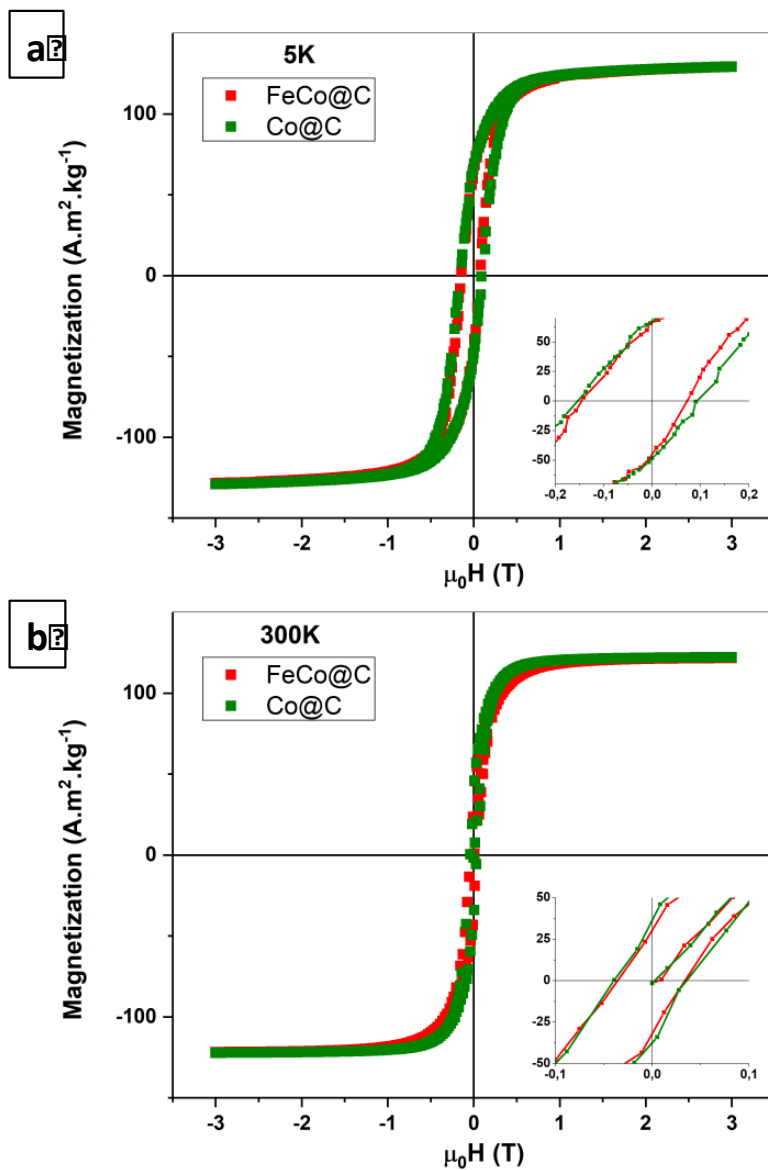of the magnetic properties which are likely to result from carbon incorporation.

Figure 4. Hysteresis loops measured by VSM on FeCo@C (red) and Co@C (green) at 5 (a) and

300 K (b) with zoomed region between -0.1 and 0.1 T.

    The heating power of **FeCo@C** and **Co@C** was determined by calorimetry using our previously

described procedure (see SI, section S7).[7,43,44] The specific absorption rate (SAR) was determined

in ethanol due to the relatively good dispersibility of the NPs in this solvent (see SI, Figure S12).

In both cases, the NPs start to heat after application of a $\mu_0 H_{rms}$ of 25 mT with a f of 93 kHz, with a quasi-linear increase of SAR with the field amplitude, reaching 165 $W \cdot g^{-1}$ in the case of **FeCo@C** and 70 $W \cdot g^{-1}$ for **Co@C** (see SI, Figure S8). These values are much lower than the previous ones reported in literature of 1600 $W \cdot g^{-1}$ for FeCo alloys at 47 mT, 100 kHz.[8,10,45] This is in agreement with the lower Ms and the lower coercivity of these particles compared to reduced FeCo and CoNPs and are likely due both to the incorporation of carbon into the particles and their partial surface oxidation. In addition, the particles lack the necessary mobility allowing the formation of chains which is responsible for the enhancement of the heating power of FeC and FeCo NPs.[10,46,47] However, the measured SAR values can be explained if we consider a metallic core of the NPs. As a whole, despite the lower SAR, the heating properties of **FeCo@C** and **Co@C** are suitable to heat the system and reach the required high temperatures under catalytic conditions (vide infra).

2. Catalytic studies

<u>Medium temperature catalysis</u>

Sabatier Reaction.

In a previous work, the catalyst used for the magnetically induced CO_2 hydrogenation into CH_4 was prepared by thermal decomposition of bis(1,5-cyclooctadiene)nickel(0), Ni(COD)$_2$, in the presence of $Fe_{2.2}C$ NPs or a combination of $Fe_{2.2}C$ NPs and Co nano-rods (Co NRs) supported on SiRAlOx.[11] The best catalytic results (CO_2 conversions of 90% with a 100% selectivity to CH_4 at a $\mu_0 H_{rms}$ of 16 mT and a f of 300 kHz) were obtained by using a mixture of Co NRs and $Fe_{2.2}C$ NPs. Here, the softer $Fe_{2.2}C$ NPs act as pre-heating agents, which activate the Co NRs that have a higher anisotropy (shape and magnetocrystalline) and Tc (> 1000 ºC) and require higher values of

magnetic field amplitude to be activated in magnetic heating. Upon pre-heating the Co-NRs, their coercive field decreases which renders them active as heating agents. Following these results, 10 wt % Ni NPs were deposited on the surface of the carbon-coated heating agent by decomposition of Ni(COD)$_2$ in the presence of **FeCo@C** (5wt% in metal; see Experimental part, section 5). This composition (**FeCo@C/Ni**) has been used in a continuous flow CO$_2$ hydrogenation using a 1:4 CO$_2$:H$_2$ molar ratio (20 mL·min^{-1} of H$_2$ and 5 mL·min^{-1} CO$_2$). 96 % of CO$_2$ conversion with a 98 % selectivity into CH$_4$ was obtained at a magnetic field intensity $\mu_0 H_{rms}$ = 32 mT and a frequency f = 300 kHz (Figure 5, Table 1). Decreasing the field amplitude led to lower conversions (91 % at $\mu_0 H_{rms}$ 28 mT, 98 % selectivity and 55 % at $\mu_0 H_{rms}$ 23 mT with 61% selectivity). The sample exhibited a reproducible cyclability over 4 hours and the catalyst was stable for more than 7 hours (Figure 5). Although higher magnetic field amplitudes were required to achieve the optimal catalytic conditions than in the case of the Fe$_{2.2}$C NPs-Ni/SiRAlOx system previously reported, it should be highlighted that no activation step was required despite the low values of SAR, which might be related to the higher Tc of Co and FeCo. The temperature of the system, measured by an ultrathin thermocouple directly located in the catalytic bed,[48] increased with the field amplitude from 230°C at 23 mT to 315 °C at 32 mT. TEM observation showed that the size of **FeCo@C/Ni** slightly increased up to *ca.* 16 nm after 7.5 hours time on stream (TOS) (Figure 5d-e). EDX analysis of **FeCo@C/Ni** after catalysis shows signals corresponding to discrete FeCo particles, indicating the good stability of the heating agents during catalysis. Ni NPs were homogeneously dispersed thorough the material and did not exhibit extended agglomeration, which may be due to the global low temperature in the system (Figure 5d-e). Therefore, **FeCo@C/Ni** has demonstrated to be an active and stable catalyst capable to carry out magnetic induced methanation without the necessity of an activation step. The most important aspect is that despite the lack of mobility of

the encapsulated nanoparticles, they are able to heat efficiently and do not experience a massive sintering at these temperatures, as was observed in the same "naked" MagNPs.[10]
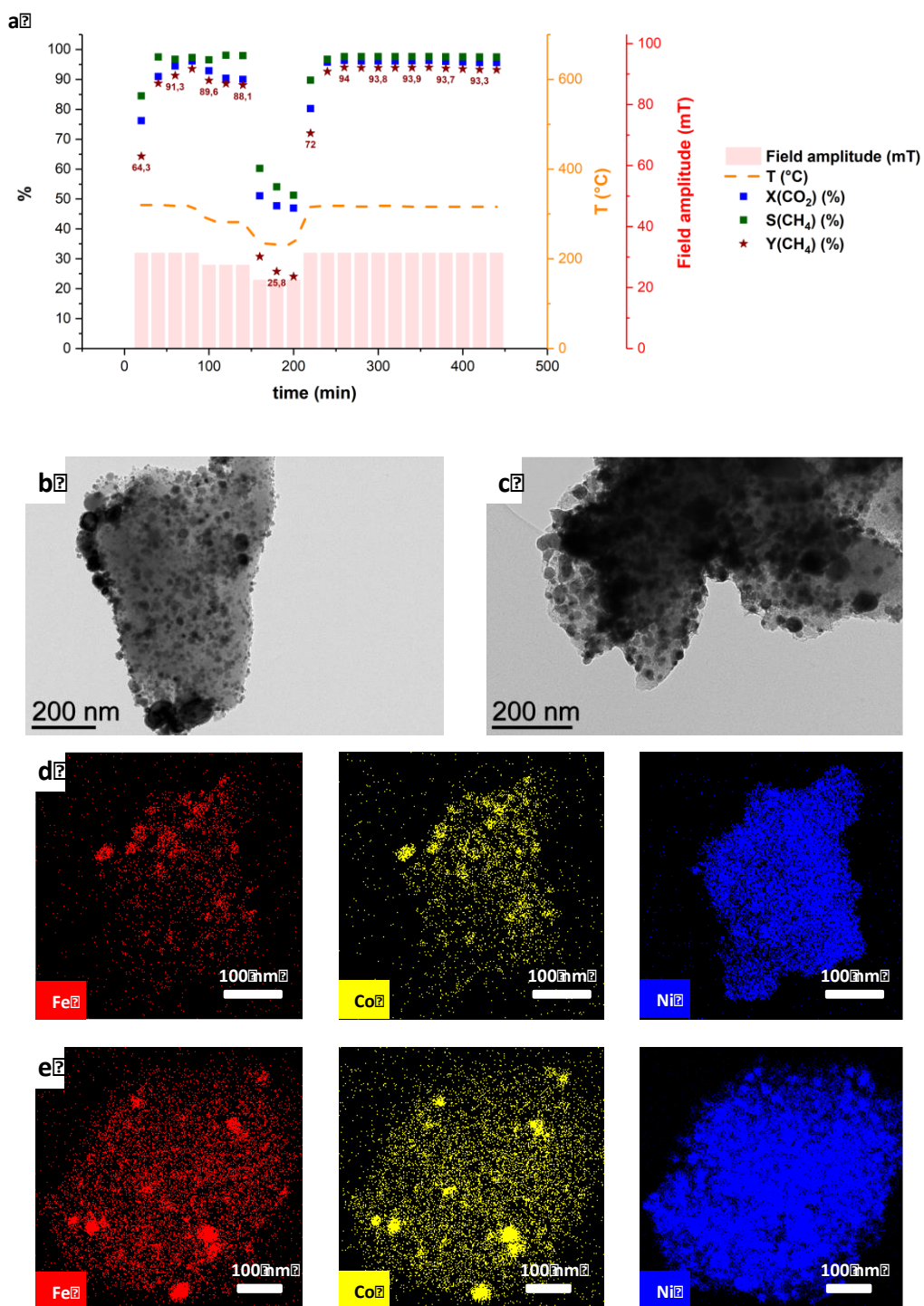

Figure 5. Catalysis of Sabatier reaction using FeCo@C/Ni. Gas flow: 25 ml/min CO_2:H_2 (1:4). X = conversion, S = selectivity and Y = yield. (a) Catalytic performances over time, (b) TEM

observation before and (c) after 7.5 hours TOS. (d) EDX mapping of Fe (red), Co (yellow) and Ni (blue) after preparation and (e) after 7.5 hours on stream. Temperature was recorded by an ultrathin thermocouple directly located in the catalytic bed and confirmed by IR thermometry.[48]

High temperature catalysis

Propane dehydrogenation (PDH).

Due to the high *Tc* values of both **Co@C** and **FeCo@C** systems, we then decided to evaluate them as heating agents for endothermic reactions operating at high temperatures.[10] With the intention to reach the highest reaction temperature, a mixture of 2:1 **FeCo@C:Co@C** was used as heating agent. Following our previous observations, FeCo would act as the *soft* material displaying higher SAR values, whose role would be to activate *hard* Co, which possesses a Tc above 1000 ºC. Thus, we experimentally observed that a mixture of 2:1 **FeCo@C:Co@C** was the optimum composition for the heating agent to activate catalysis at high temperatures. Concerning the catalyst we chose Pt/Sn, prepared by a recently published procedure,[10] since recent works have demonstrated that Sn not only can enhance the activity of Pt NPs in propane dehydrogenation, but also can improve the selectivity and stability of the catalyst.[24,49-50] Therefore, Pt NPs (0.35 wt %) promoted with Sn (0.5 wt %)[52] were supported on a mixture of 2:1 **FeCo@C:Co@C** (see Experimental part, section 5) and used as catalyst in Propane Dehydrogenation (PDH) (>700°C). By using an incoming gas of pure C_3H_8 (flow of 20 mL·min^{-1}), the conversion reached values up to 11% with 81% selectivity to propene at *μ₀Hrms* 65mT (300 kHz) and a monitored temperature of 620 °C (Figure 6a; Table 1). The remaining 19 % of selectivity is due to the formation of methane and propane in a ratio 1:1. When only **FeCo@C** was used as heating agent in the same conditions significant lower performances were obtained (see SI, Figure S13). TEM observations demonstrated that **FeCo@C** and **Co@C** were stable in time as their sizes slightly increased up to

ca. 15 nm after 2 hours TOS (Figure 6b-c, SI). EDX analysis of the sample before catalysis could not clearly identify Pt and Sn due to the low signal as a result of the low catalyst loadings. However, EDX analysis after catalysis indicates that a slight agglomeration of Pt and Sn, mostly located on the heating agents, has taken place (Figure 6d). Similar aggregations of Pt over the heating agents has been also observed in other high temperature magnetically induced catalytic reactions.[10,53] Under the same conditions, uncoated FeCo NPs while being able of activating PDH catalysis with slightly higher activity, have limited stability due to massive sintering of metallic NPs and carbon deposition.[10] Therefore, the main advantage of carbon encapsulation is the stabilization of the catalytic system, avoiding sintering of the heating agents.
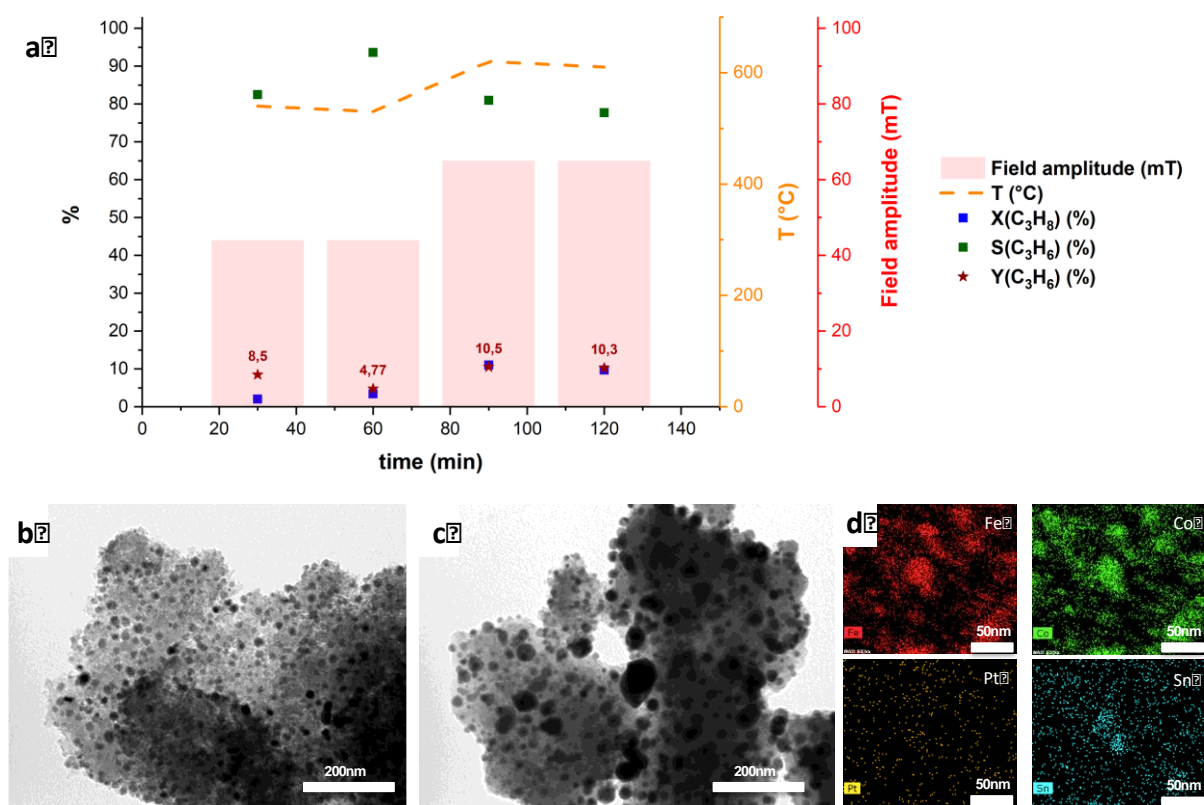

Figure 6. *PDH* reaction using 2 :1 **FeCo@C:Co@C/PtSn** (Pt 0.35 wt %, Sn 0.5 wt %) as catalyst. Gas stream: 20 ml/min C_3H_8. X = conversion, S = selectivity and Y = yield. (a) Catalytic

performances over time, (b) TEM observation before and (c) after 4.5 hours TOS. (d) EDX mapping of Fe (red), Co (green), Pt (yellow) and Sn (blue) after 4.5 hours on stream. Temperature was recorded by an ultrathin thermocouple directly located in the catalytic bed and confirmed by IR thermometry.[48]

Propane Dry reforming (PDR)

Propane Dry Reforming (PDR) was performed by using Ni (10 wt %) impregnated on 2:1 **FeCo@C:Co@C** as catalyst (**FeCo@C:Co@C/Ni;** see Experimental part, section 5). At $\mu_0 H_{rms}$ 32 mT (300 kHz), 9% of the incoming propane was converted into CO and H_2 with 100% selectivity using a gas flow of 10 mL·min^{-1} (3:1 molar ratio CO_2:C_3H_8). However, upon increasing the field amplitude to 60 mT, propane conversion was increased to 54% with a 97% selectivity to CO, very close to the conversion value at the thermodynamic equilibrium (Figure 7, Table 1).[54] The conversion values observed can be explained by the temperature increase from 425°C to 620°C, upon increasing the field amplitude. The selectivity toward CO is particularly high. We propose that this behaviour is related to the encapsulation of FeCo and Co NPs and successful prevention of parallel reactions such as Fischer Tropsch, which is a typical undesired side-reaction.[55] The temperature of the system remained stable during the 2.5 hours of the catalytic test. The size of the MagNPs showed again a slight increase after 2 hours TOS (ca. 14 nm). EDX analysis after catalysis revealed that Ni catalyst NPs slightly migrated toward the heating agents (Figure 7b-e), but keeping a good size distribution.
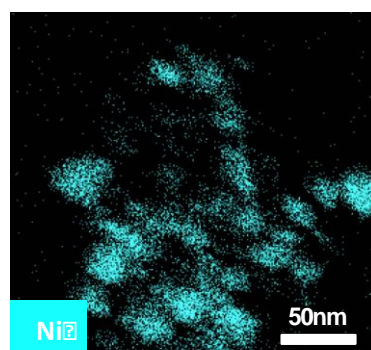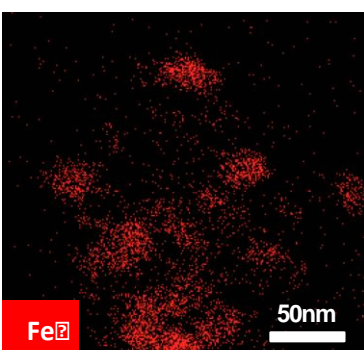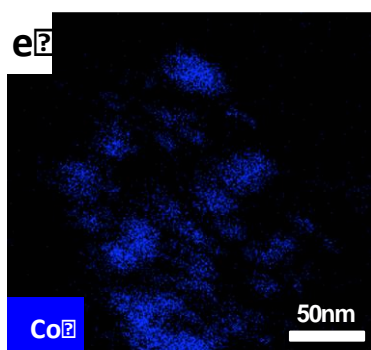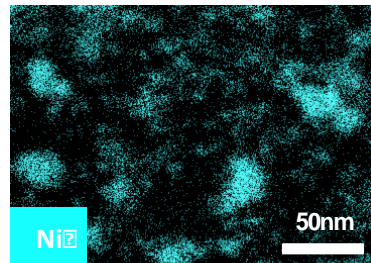
a

b

c

d

e
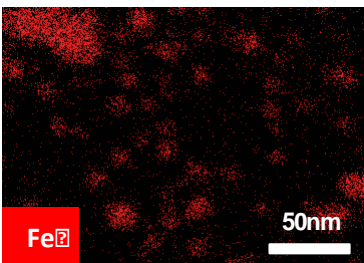
Figure 7. *PDR* reaction using 2 :1 **FeCo@C:Co@C/Ni** (10 wt %) as catalyst. Gas stream: 10 ml/min CO_2:C_3H_8 (3:1). X = conversion, S = selectivity and Y = yield. (a) Catalytic performances over time, (b) TEM observation before and (c) after 2 hours TOS. (d) EDX mapping of Fe (red), Co (b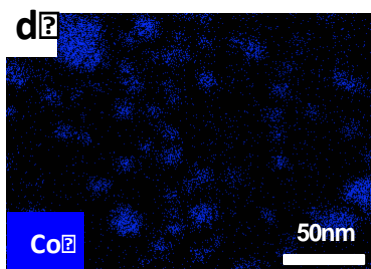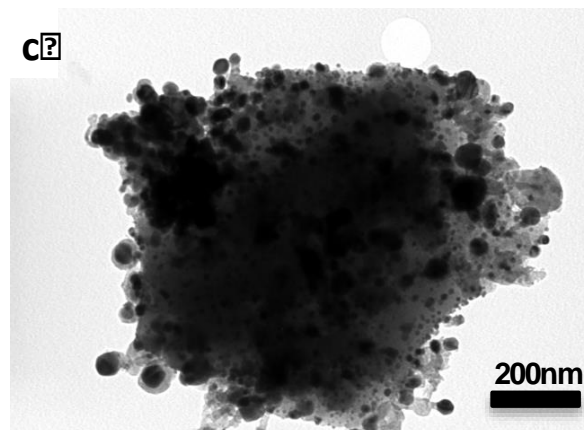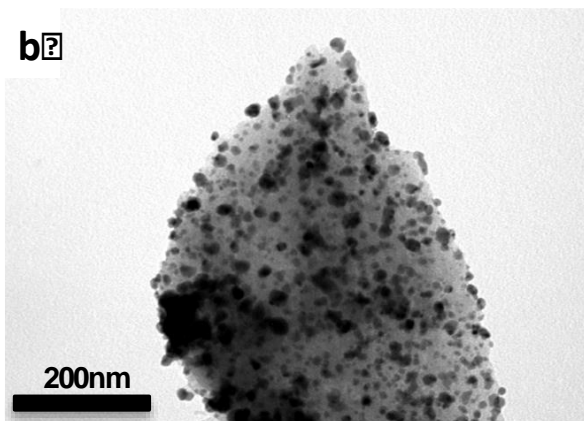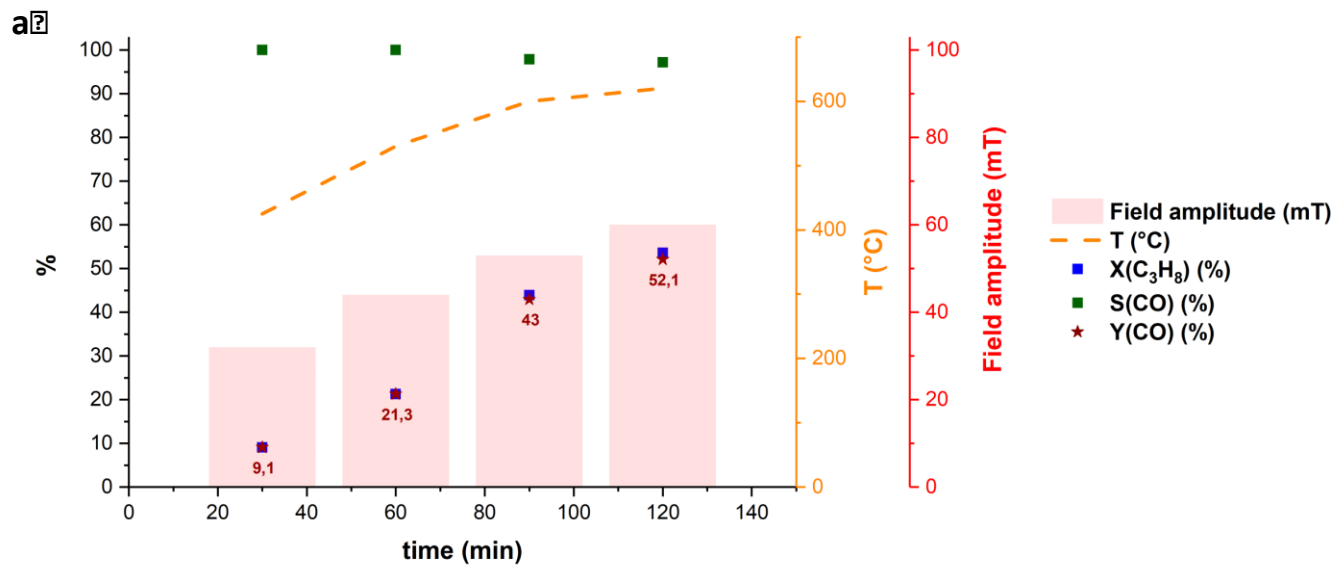lue), Ni (light blue) after preparation and (e) after 2 hours on stream. Temperature was recorded by an ultrathin thermocouple directly located in the catalytic bed and confirmed by IR thermometry.[48]

Table 1. Magnetic induced catalysis performances of Sabatier, Propane Dry Reforming (PDR) and Propane DeHydrogenation (PDH) using **FeCo@C** and **Co@C** as heating agents.

Reaction	Heating Agent (HA)	HA loading (%wt)	Catalyst nature	Catalyst loading (%wt)	Field amplitude (mT) [a]	X: Conversion (%)	S: Selectivity (%)	T_{bulk} (°C)	Conversion at thermodynamic Eq. (%).[b]
						$X(CO_2)$	$S(CH_4)$		
Sabatier	FeCo@C	5	Ni	10	23	48,6	55,2	235	99
					28	91,1	97,5	280	96
					32	96	97,5	315	94
						$X(C_3H_8)$	$S(CO)$		
PDR	FeCo@C Co@C	5	Ni	10	32	9,1	100	425	15
					44	21,3	100	530	37
					53	43,9	97,9	600	60
					60	53,6	97,2	620	72
						$X(C_3H_8)$	$S(C_3H_6)$		
PDH	FeCo@C Co@C	5	Pt Sn	0,35 0,5	44	2,7	88,1	530	27
					65	10,4	79,4	620	52

[a] Magnetic field applied of 300 KHz.

[b] Conversions at thermodynamic equilibrium were estimated employing the Gibbs free energy minimization method.[48,56-58]

[c] Temperatures were measured by an ultrathin thermocouple directly located in the catalytic bed and validated with an IR camera. Notice that temperatures given are an estimation and the real temperatures at the surface of the catalyst are probably higher.

2. Stability studies

In order to investigate in more detail the stability of our heating agents and of the catalyst under the harsh conditions employed, we ran PDR over 6 hours. Specifically, we tested 2:1 FeCo@C:Co@C/Ni (10 wt% of Ni) and a gas mixture of 3:1 CO_2:C_3H_8 with a total flow rate of 10 mL·min^{-1} during 6 hours. We previously showed that after two hours on stream, 52 % yield could be reached with nearly 100% selectivity for CO, while supported Ni NPs were slightly agglomerated. Two more cycles with variable magnetic field amplitudes (32 mT, 44 mT, 53 mT, 60 mT) were performed and enabled to show a quasi-perfect cyclability in terms of temperature reached by magnetic induction of the heating agents (up to 620°C, at μ_0H_{rms} 60 mT, 300 kHz) and CO yields (Figure 8). This result demonstrates the very efficient encapsulation of the FeCo@C and Co@C even at high temperatures. The catalytic performances of the sample remained stable and reproducible for all the field amplitudes tested. However, EDX mapping after 6 hours on stream shows a more important agglomeration of the Ni NPs, which, however, did not induce any significant decrease of the catalytic performances (see SI, Figure S14a-c). Then, the sample was exposed to air and another reaction cycle was performed. This led to a slight decrease of the temperature reached in the system to 605°C at a μ_0H_{rms} 60 mT, but no significant effects on the catalytic performances were observed. In addition, the morphology of the sample was not significantly altered upon air exposure followed by two additional hours on stream (see SI, Figure S14d). These results demonstrate the encapsulation in carbon, which remediates the catalyst instability issues associated to the sintering of MagNPs under high temperature catalysis.
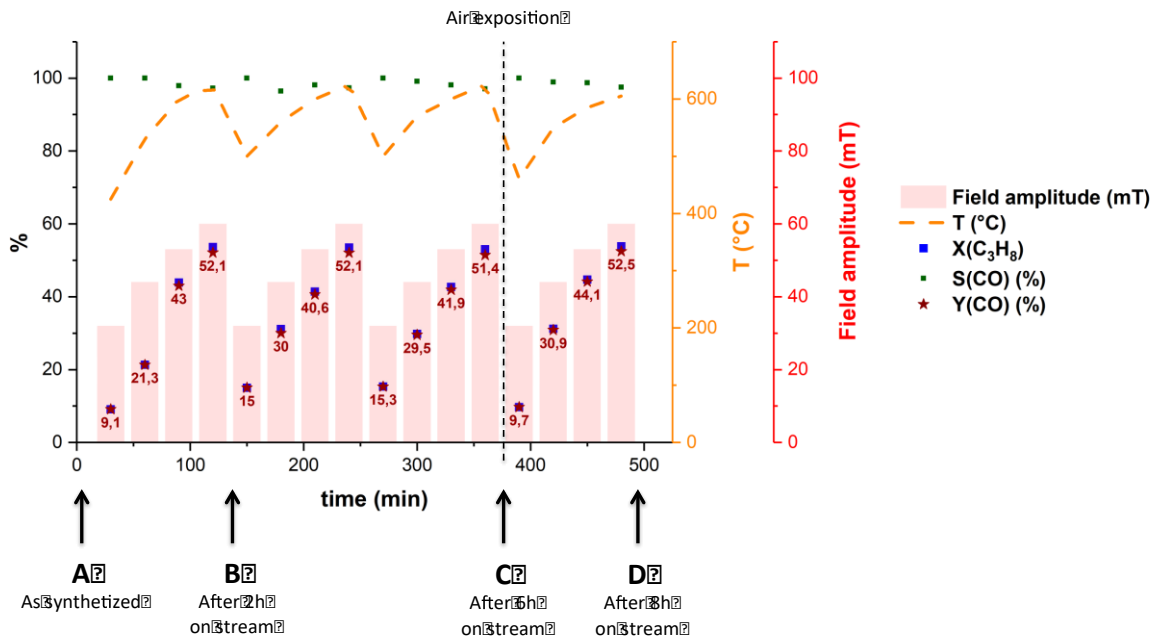
Figure 8. Magnetically induced Propane Dry Reforming (PDR) performances and temperatures using 2 :1 **FeCo@C:Co@C/Ni** (10 wt %) as catalyst at variable magnetic field amplitudes. Gas stream: 10 ml/min CO_2:C_3H_8 (3:1). X = conversion, S = selectivity and Y = yield. Temperature was recorded by an ultrathin thermocouple directly located in the catalytic bed and confirmed by IR thermometry.[48]

Conclusions

Magnetically induced catalysis can indeed address various reactions and temperature ranges. Though the weakness of this technique is the agglomeration of the heating magnetic nanoparticles upon magnetic excitation, we have shown that this problem can be circumvented by confining the heating NPs in carbon. Thus, we have successfully encapsulated magnetic FeCo and Co NPs in carbon (Co@C and FeCo@C), which leads to ultra-stable heating agents suitable for high temperature magnetically-induced catalysis. Combining a series of characterization techniques such as HRTEM, EDX, XRD, XPS and VSM, we can conclude that Co@C and FeCo@C NPs

have a metallic core and an oxidized surface encapsulated by a carbon layer, but that under reductive conditions similar to those used in the catalytic experiments, the oxidized surface is reduced.

Catalytic studies have shown that medium (Sabatier 300-400 °C) and high temperature (PDR and PDH >600 °C) catalysis can be activated by FeCo@C or a mixture of FeCo@C:Co@C (2:1) with Ni or Pt-Sn supported, with consistent conversions and selectivities compared to traditional heating sources. Under the conditions employed, we observed a good stability of the heating agents, in terms of temperature, and of the catalyst as a whole in terms of catalytic performances. However, a systematic agglomeration of the catalytic NPs (PtSn or Ni NPs) was observed at high temperature as in classical heterogeneous catalysis. Under the same conditions, the use of naked FeCo NPs in PDR or PDH did not show stability for more than one hour.[10] Thus, the encapsulation of the heating agent constitutes a major improvement toward the development of stable catalysts for high temperature magnetically-induced catalysis.

Finally, in the case of PDR, the catalyst showed remarkable cyclabilities of temperature and catalytic performance, up to 4 times over at least 6 hours. Furthermore, excellent cyclability was achieved even after exposure to air of the catalysts and/or partial sintering of the Ni NPs.

Experimental Part

1. General considerations and starting materials

Most of operations were carried out using standard Schlenk tubes, Fischer–Porter bottle techniques or in a glove-box under argon atmosphere. Mesitylene, toluene and tetrahydrofurane (THF) were obtained from VWR Prolabo, then purified on alumina desiccant and degassed by bubbling Ar through the solution for 20 minutes. The commercial products, hexadecylamine

(HDA, 99%), Ni(COD)$_2$, (COD = cyclo-octadiene) and Bu$_3$SnH (1M in cyclohexane) were obtained from Sigma-Aldrich. Pt$_2$(dba)$_3$, [Fe{N(SiMe$_3$)$_2$}$_2$]$_2$ and [Co{N(SiMe$_3$)$_2$}$_2$(THF)] precursors were obtained from Nanomeps. All the commercial compounds were used as received. All gasses were supplied by Air-Liquide with the following purity: CO$_2$ Alphagaz N48, H$_2$ N55, Ar N56, CH$_4$ N55.

Transmission Electron Microscopy (TEM) and High resolution TEM (HRTEM). FeCo NPs, Co NPs, FeCo/C, Co/C, FeCo@C and Co@C NPs were observed by TEM and HRTEM after deposition on a copper grid of a drop of a suspension of the material in THF. TEM analyses were performed at the "Servicio de Microscopía Electrónica" of Universitat Politècnica de València (UPV) by using a JEOL JEM 1010 CX-T electron microscope operating at 100 kV with a point resolution of 4.5 Å. The approximation of the particles mean size was made through a manual analysis of enlarged micrographs by measuring a number of particles on a given grid. HRTEM measurements were performed using a JEOL 2100F microscope operating at 200 kV, both in transmission (TEM) and scanning-transmission modes (STEM). Energy-dispersive X-ray spectrometry (EDX) and STEM images were obtained using a high-angle annular dark-field detector (HAADF), which allows Z-contrast imaging. FFT treatments have been carried out with Digital Micrograph Version 3.7.4.

Inductively Coupled Plasma (ICP): ICP analyses of FeCo@C and Co@C were performed by ICP technique service of the Instituto de Tecnología Química (ITQ), using a Varian 715-ES ICP-Optical Emission Spectrometer. The samples for ICP were prepared following a digestion method recently reported.[59] In particular, 30 mg of catalyst sample were suspended in 21 mL HCl-HNO$_3$ (6:1). The solution was then sonicated for 90 minutes and the samples were digested at 180ºC for

15 hours. Then, the solution was cooled down to room temperature (r.t.), diluted with 100 mL of water and analyzed by ICP.

RAMAN: Raman spectra were recorded using an excitation of 785 nm in a Renishaw In via Raman spectrometer equipped with a Lyca microscopy. The samples (powder) were deposed on an Al support, and measured in the region between 0 and 3000 cm^{-1} with a resolution of < 4 cm^{-1}.

X-Ray Photoelectron Spectroscopy (XPS): XPS analyses were performed using a SPECS device equipped with a Phoibos 150-9MCD detector using Mg-Kα radiation (hν= 1235.6 eV) and Al-Kα radiation (hν= 1483.6 eV) from a dual source. The pressure during the measurements was kept under 10^{-9} Torr. The quantification and titration of the spectra was done with the help of the software CASA, referencing them in base of C1s = 284.5 eV.

X-ray Powder Diffraction (XRD): Powder samples were analysed using a Cubix-Pro PANalytical diffractometer equipped with a detector PANalytical X´Celerator, employing a X-Ray monochromatic radiation of CuKα (λ_1=1.5406 Å, λ_2=1.5444 Å, I$_2$/I=0.5).

Temperature-Programmed Reduction (TPR): Micromeritics Auto-Chem 2910 catalyst characterization system with a thermal conductivity detector (TCD) was used for TPR analysis. Before analysis of the samples (50 mg), they were pretreated at room temperature in flowing He (10 mL/min) for 20 min. Then, the samples were heated from 25 ºC to 600 ºC at a rate of 5 ºC/min in a flow (50 mL/min) of H$_2$ in Ar (10 % vol.).

Gas Chromatography coupled to Mass Spectrometry (GC-MS): GC-MS analyses were carried out in a PerkinElmer 580 Gas Chromatograph equipped with a TCD detector and coupled to a Clarus SQ8T Mass Spectrometer. Reactants conversions, and product yields and selectivities were calculated by performing a C balance to the chromatograms. The areas of each peak were corrected with their response factor obtained after calibration of the TCD detector.

Vibrating-sample magnetometer (VSM): Magnetic measurements were performed on a Vibrating Sample Magnetometer (VSM, Quantum Device PPMS Evercool II). VSM studies were carried out on compact powder samples that were prepared and sealed under argon atmosphere.

2. Synthesis of FeCo and Co NPs

The FeCo NPs were prepared according to literature.[60] Fe and Co precursors, [Fe{N(SiMe₃)₂}₂]₂ (180,7 mg; 0.2 mmol) and [Co{N(SiMe₃)₂}₂(THF) (150.5 mg; 0.4 mmol)], were reduced under 3 bar of H_2 upon heating at 150 °C for 24 h in mesitylene (20 mL) and in the presence of long chain surfactants, hexadecylamine (HDA; 386 mg; 1.6 mmol), and hexadecylamine hydrochloride (HDA·HCl; 333.5; 1.2 mmol), The precursors concentrations were kept at 20 $mmol·L^{-1}$. The HDA and HDA·HCl concentrations were 80 and 60 $mmol·L^{-1}$, respectively. After reaction, a black solution with the magnetic FeCo NPs stabilized by HDA/HDA·HCl was obtained. A drop of this solution was deposed on a cooper grid, and the size of the NPs was measured by TEM for at least 100 nanoparticles, which afforded a mean value of 10.7 ± 2.4 nm (Figure S1). ICP: Fe: 2.6 wt% and Co 2.3 wt%.

Co NPs: Cobalt NPs were prepared as described for FeCo NPs but starting from the Co precursor, [Co(N(Si(CH₃)₃)₂)₂,THF] (361,4 mg ; 0.8 mmol). The size of the NPs was measured by TEM for at least 100 nanoparticles, which afforded a mean value of 11.7 ± 2.6 nm (Figure S2). ICP: Co: 4.8 wt%.

3. Synthesis of FeCo@C and Co@C NPs

FeCo@C: 920 mg of activated carbon dispersed in 10 mL of mesitylene were added to a Fischer−Porter bottle charged with a suspension of FeCo NPs (78 mg) in 20 mL of mesitylene. After 24 h of vigorous stirring, FeCo NPs were adsorbed on the activated carbon forming FeCo/C

(see SI, Figure S3). Then, FeCo/C was washed with hexane three times, and dried at 60 ºC overnight. The resulting black powder was then subjected to a pyrolysis process (2 h at 600 ºC under N_2 pressure, with a heating ramp: 10 ºC·min^{-1}), producing the FeCo NPs encapsulated in carbon (FeCo@C). The size of the NPs was measured by TEM for at least 100 nanoparticles, which afforded a mean value of 10.8 ± 3.2 nm (Figure 2a-c).

Co@C: Co@C was prepared as described for FeCo@C but using a suspension of Co NPs (76 mg) in 20 mL. The size of the NPs was measured by TEM for at least 100 nanoparticles, which afforded a mean value 10.7 ± 2.4 nm (Figure 2d-f).

4. Synthesis of FeCo@C and Co@C decorated with Ni and PtSn NPs.

FeCo@C/Ni and FeCo@C-Co@C/Ni catalyst (10% Ni loading) were prepared by the decomposition of Ni(COD)$_2$ in the presence of FeCo@C or FeCo@C:Co@C (2:1) in mesitylene. In a typical preparation 156 mg Ni(COD)$_2$ were dissolved in 20 mL mesitylene and 300 mg FeCo@C or FeCo@C:Co@C (2:1) were added to the solution. The mixture was then heated at 150 °C under Ar atmosphere and vigorous stirring during 1 h followed by 3 washing steps with toluene. Drying under vacuum enables to get Ni NPs with a mean size of cs. 2-4 nm immobilized on FeCo@C or FeCo@C:Co@C (2:1). Total amount of collected powder was of ca. 350 mg.

FeCo@C/Pt-Sn and FeCo@C:Co@C/Pt-Sn. Were prepared by adapting a published procedure.[10] For Pt-Sn catalysts (0.5% loading), the catalyst was prepared by mixing preformed Pt NPs with FeCo@C or a mixture of FeCo@C:Co@C (2:1). In a typical preparation, 6,5 mg of Pt$_2$(dba)$_3$ in 5 ml of THF are stirred in the presence of 1 bar CO for 20 minutes. The dark brown mixture formed is evaporated to a small volume (1-2 ml). Complete drying has to be avoided in order to facilitate re-dispersing nanoparticles. Three washing steps by pentane are then performed

before diluting the obtained NPs in 10ml THF. Then, Bu₃SnH is added to the suspension of the Pt

NPs and the solution is let under magnetic stirring for 5 to 10 minutes. Finally, 450 mg of FeCo@C

or 2:1 FeCo@C:Co@C are added and the solution is stirred for 10 minutes. The solvent is

eliminated while sonicating to obtain a fine dark brown powder that is collected and stored.

5. Catalytic reactions.

Catalytic experiments were performed in a quartz tube continuous-flow reactor of 1 cm diameter

which was placed at the centre of an inductor delivering an AC magnetic field oscillating at a

frequency of 300 kHz with a root-mean-square (rms) amplitude adjustable between 0 and 65mT.

The induction coil is 3 cm wide and 2 cm high. We systematically used 400 mg of catalytic bed

for Sabatier reaction and between 800-1.200 mg of catalytic bed for PDH and PDR (800 mg

FeCo@C/Ni or FeCo@C/Pt-Sn + 400 mg Co@C/Ni or Co@C/Pt-Sn). Mass flows of C_nH_{2n+2}:CO_2

1:3 and 1:1 with 10 mL·min⁻¹ C_nH_{2n+2} were supplied at the inlet for PDR and for MDR respectively

(Weight hourly space velocity, WHSV, 7.5 L·h⁻¹·$g_{(Ni)}$⁻¹). 20 mL·min⁻¹ pure propane was supplied

for PDH (WHSV 300 L·h⁻¹·$g_{(Pt)}$⁻¹). For the Sabatier reaction 25 mL·min⁻¹ of a 4:1 H_2:CO_2 molar

mixture were flowed (WHSV 37.5 L·h⁻¹·$g_{(Ni)}$⁻¹). The outgoing gases are injected in a Gas

Chromatography–Mass Spectrometry (PerkinElmer 580 Gas Chromatograph-Thermal

Conductivity Detector coupled to a Clarus SQ8T Mass Spectrometer). Calibration of the gas

injection and the GC analysis method have been performed with pure gases. The response factor

of the analytes i RF_i is determined by injecting known quantities of each analyte i into the column.

The area of the peak of the specie i on the chromatogram (A_i) enables to determine the conversion

of i (X_i) and selectivity toward j (S_j) based on the calculations below (case of dehydrogenation of

propane). For dry reforming of alkanes, the conversion is calculated on the alkane basis, as CO_2 is expected to be supplied in excess.

Propane → Propylene + Ethane + Methane
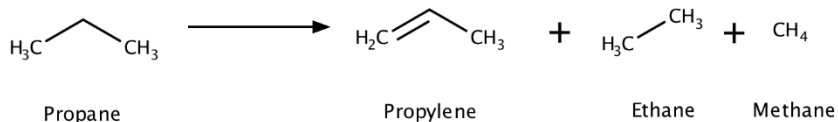
$$X_{propane} = \frac{\sum_{products} RF_{Product,i} \cdot A_{Product,i}}{\sum_{products} RF_{Product,i} \cdot A_{Product,i} + \sum_{reactant} RF_{reactant,i} \cdot A_{reactant,i}}$$

$$S_{propylene} = \frac{RF_{Propylene} \cdot A_{Propylene}}{\sum_{products} RF_{Product,i} \cdot A_{Product,i}}$$

6. Digestion experiments.

Following a similar procedure as Bao and co-workers[33] who concluded about CoNi NPs that they were completely encapsulated by graphene because they were not soluble in a strong acid, we demonstrated that the carbon layer of FeCo@C and Co@C is discontinuous. Specifically, Co and FeCo NPs encapsulated in carbon (10 mg of FeCo@C/Co@C) were practically dissolved in a H_2SO_4 solution (2M, 5 ml) at 80 ºC after 2 h. Analyzing by ICP-AES the resulting solutions we observed a metal content of 3.55 wt % Co for Co@C, and 2.45 wt % Co; 2.71 wt % Fe for FeCo@C.

Supporting Information

Composition, morphology and structure of carbon encapsulated Magnetic Nanoparticles (**FeCO@C** and **Co@C**); TEM, STEM-HADDF and EDX; XRD; Raman; TPR; XPS; SAR (T) measurements for **Co@C** and **FeCO@C**; detailed catalytic results of PDH using **FeCo@C/PtSn**; **FeCo@C:Co@C/Ni** STEM-EDX micrographs during PDR reaction.

References

[1] Ceylan, S.; Friese, C.; Lammel, C.; Mazac, K.; Kirschning, A. Inductive Heating for Organic Synthesis by Using Functionalized Magnetic Nanoparticles Inside Microreactors. *Angew. Chem. Int. Ed.* **2008,** *47*, 8950-8953.

[2] Ceylan, S.; Coutable, L.; Wegner, J.; Kirschning, A. Inductive Heating with Magnetic Materials inside Flow Reactors. *Chem. Eur. J.* **2011**, *17*, 1884-1893.

[3] Houlding, T. K.; Gao, P.; Degirmenci, V.; Tchabanenko, K.; Rebrov, E. V. Mechanochemical synthesis of TiO2/NiFe2O4 magnetic catalysts for operation under RF field. *Mater. Sci. Eng.: B* **2015**, *193*, 175-180.

[4] Asensio, J. M.; Miguel, A. B.; Fazzini, P.-F.; van Leeuwen, P. W. N. M.; Chaudret, B. Hydrodeoxygenation Using Magnetic Induction: High-Temperature Heterogeneous Catalysis in Solution. *Angew. Chem. Int. Ed. **2019***, *58*, 11306-11310.

[5] Liu, Y.; Gao, P.; Cherkasov, N.; Rebrov, E. V. Direct amide synthesis over core–shell TiO_2@$NiFe_2O_4$ catalysts in a continuous flow radiofrequency-heated reactor. *RSC Adv.* **2016**, *6*, 100997-101007.

[6] Liu, Y.; Cherkasov, N.; Gao, P.; Fernández, J.; Lees, M. R.; Rebrov, E. V. The enhancement of direct amide synthesis reaction rate over TiO_2@SiO_2@$NiFe_2O_4$ magnetic catalysts in the continuous flow under radiofrequency heating. *J. Catal.* **2017**, *355*, 120-130.

[7] Meffre, A.; Mehdaoui, B.; Connord, V.; Carrey, J.; Fazzini, P. F.; Lachaize, S.; Respaud, M.; Chaudret, B. Complex Nano-objects Displaying Both Magnetic and Catalytic Properties: A Proof of Concept for Magnetically Induced Heterogeneous Catalysis. *Nano Lett.* **2015**, *15*, 3241-3248.

[8] Bordet, A.; Lacroix, L.-M.; Fazzini, P.-F.; Carrey, J.; Soulantica, K.; Chaudret, B. Magnetically Induced Continuous CO_2 Hydrogenation Using Composite Iron Carbide Nanoparticles of Exceptionally High Heating Power. *Angew. Chem. Int. Ed.* **2016**, *55*, 15894-15898.

[9] Mortensen, P. M.; Engbæk, J. S.; Vendelbo, S. B.; Hansen, M. F.; Østberg, M. Direct Hysteresis Heating of Catalytically Active Ni–Co Nanoparticles as Steam Reforming Catalyst. *Ind. Eng. Chem. Res.* **2017**, *56*, 14006-14013.

[10] Marbaix, J.; Mille, N.; Lacroix, L. M.; Asensio, J. M.; Fazzini, P. F.; Soulantica, K.; Carrey, J.; Chaudret, B. *ACS Appl NanoMat.* **2020**, *3*, 3767-3778.

[11] Vinum, M. G.; Almind, M. R.; Engbæk, J. S.; Vendelbo, S. B.; Hansen, M. F.; Frandsen, C.; Bendix, J.; Mortensen, P. M. Dual-Function Cobalt–Nickel Nanoparticles Tailored for High-Temperature Induction-Heated Steam Methane Reforming. *Angew. Chem. Int. Ed.* **2018**, *57*, 10569-10573.

[12] Kale, S. S.; Asensio, J. M.; Estrader, M.; Werner, M.; Bordet, A.; Yi, D.; Marbaix, J.; Fazzini, P.-F.; Soulantica, K.; Chaudret, B. Iron carbide or iron carbide/cobalt nanoparticles for magnetically-induced CO_2 hydrogenation over Ni/SiRAlOx catalysts. *Catal. Sci. Technol.* **2019**, *9*, 2601–2607.

[13] Varsano, F.; Bellusci, M.; La Barbera, A.; Petrecca, M.; Albino, M.; Sangregorio, C. Dry reforming of methane powered by magnetic induction. *Int. J. Hydrog. Energ.* **2019**, *44*, 21037-21044.

[14] Wang, W.; Duong-Viet, C.; Xu, Z.; Ba, H.; Tuci, G.; Giambastiani, G.; Liu, Y.; Truong-Huu, T.; Nhut, J.-M.; Pham-Huu, C. CO_2 methanation under dynamic operational mode using nickel nanoparticles decorated carbon felt (Ni/OCF) combined with inductive heating. *Catal. Today* **2019**, DOI: doi.org/10.1016/j.cattod.2019.02.050.

[15] Benkowsky, G. *Induktionserwärmung: Härten, Glühen, Schmelzen, Löten, Schweißn: Grundlagen und praktische Anleitungen für Induktionserwärmungsverfahren, insbesonere auf dem Gebiet der Hochfrequenzerwärmung*, 5th ed.; Verlag Technik: Berlin, 1990; p 12.

[16] Carrey, J.; Mehdaoui, B.; Respaud, M. Simple models for dynamic hysteresis loop calculations of magnetic single-domain nanoparticles: Application to magnetic hyperthermia optimization. *J. Appl. Phys.* **2011**, *109*, 83921.

[17] Khodakov, A. Y.; Chu, W.; Fongarland, P. Advances in the Development of Novel Cobalt Fischer−Tropsch Catalysts for Synthesis of Long-Chain Hydrocarbons and Clean Fuels. *Chem. Rev.* **2007**, *107*, 1692-1744.

[18] Liu, J.; Guo, Z.; Childers, D.; Schweitzer, N.; Marshall, C. L.; Klie, R. F.; Miller, J. T.; Meyer, R. J. Correlating the degree of metal–promoter interaction to ethanol selectivity over MnRh/CNTs CO hydrogenation catalysts. *J. Catal.* **2014**, *313*, 149-158.

[19] Ghaib, K.; Nitz, K.; Ben-Fares, F.-Z., Chemical Methanation of CO_2: A Review. *Chem. Bio. Eng. Rev.* **2016**, *3*, 266-275.

[20] Cored, J.; García-Ortiz, A.; Iborra, S.; Climent, M. J.; Liu, L.; Chuang, C.-H.; Chan, T.-S.; Escudero, C.; Concepción, P.; Corma, A. Hydrothermal Synthesis of Ruthenium Nanoparticles with a Metallic Core and a Ruthenium Carbide Shell for Low-Temperature Activation of CO_2 to Methane. *J. Am. Chem. Soc.* **2019,** *141*, 19304-19311.

[21] Schiermeier, Q. Renewable power: Germany's energy gamble. *Nature* **2013**, *496*, 158.

[22] Wilhelm, D. J.; Simbeck, D. R.; Karp, A. D.; Dickenson, R. L. Syngas production for gas-to-liquids applications: technologies, issues and outlook. *Fuel Process. Technol.* **2001**, *71*, 139–148.

[23] Sattler, J. J. H. B.; Ruiz-Martinez, J.; Santillan-Jimenez, E.; Weckhuysen, B. M. Catalytic Dehydrogenation of Light Alkanes on Metals and Metal Oxides. *Chem. Rev.* **2014**, *114*, 10613–10653.

[24] Siahvashi, A.; Chesterfield, D.; Adesina, A. A. Propane CO_2 (Dry)Reforming over Bimetallic Mo-Ni/Al_2O_3 catalyst. *Chem. Eng. Sc*i. **2013**, *93*, 313–325.

[25] Lee, M. H.; Nagaraja, B. M.; Lee, K. Y.; Jung, K. D. Dehydrogenation of Alkane to Light Olefin over PtSn/Al_2O_3 Catalyst: Effects of Sn Loading. *Catal. Today* **2014**, *232*, 53–62.

[26] Liu, L.; Diaz, U.; Arenal, R.; Agostini, G.; Concepcion, P.; Corma, A. Generation of subnanometric platinum with high stability during transformation of a 2D zeolite into 3D. *Nat Mater.* **2017**, *16*, 132-138.

[27] Liu, L.; Zakharov, D. N.; Arenal, R.; Concepcion, P.; Stach, E. A.; Corma, A. Evolution and stabilization of subnanometric metal species in confined space by in situ TEM. *Nat. Commun.* **2018**, *9*, 574.

[28] Liu, L.; Gao, F.; Concepción, P.; Corma, A. A new strategy to transform mono and bimetallic non-noble metal nanoparticles into highly active and chemoselective hydrogenation catalysts. *J. Catal.* **2017**, *350*, 218-225.

[29] Liu, L.; Concepción, P.; Corma, A. Non-noble metal catalysts for hydrogenation: A facile method for preparing Co nanoparticles covered with thin layered carbon. *J. Catal.* **2016**, *340*, 1-9.

[30] Fu, T.; Wang, M.; Cai, W.; Cui, Y.; Gao, F.; Peng, L.; Chen, W.; Ding, W. Acid-Resistant Catalysis without Use of Noble Metals: Carbon Nitride with Underlying Nickel. *ACS Catal.* **2014**, *4*, 2536-2543.

[31] Garnero, C.; Lepesant, M.; Garcia-Marcelot, C.; Shin, Y.; Meny, C.; Farger, P.; Warot-Fonrose, B.; Arenal, R.; Viau, G.; Soulantica, K.; Fau, P.; Poveda, P.; Lacroix, L. M.; Chaudret, B. Chemical Ordering in Bimetallic FeCo Nanoparticles: From a Direct Chemical Synthesis to Application As Eficient High-Frequency Magnetic Materials. *Nano Lett.* **2019**, 19, 1379–1386.

[32] Lepesant, M.; Bardet, B.; Lacroix, L.-M.; Fau, P.; Garnero, C.; Chaudret, B.; Soulantica, K.; Defforge, T.; Valente, D.; Andreazza, C.; Billoué, J.; Poveda, P.; Gautier, G. Impregnation of

High-Magnetization FeCo Nanoparticles in Mesoporous Silicon: An Experimental Approach. *Front. Chem.* **2018**, *6,* 1-6.

[33] Deng, J.; Ren, P.; Deng, D.; Bao, X. Enhanced Electron Penetration through an Ultrathin Graphene Layer for Highly Efficient Catalysis of the Hydrogen Evolution Reaction. *Angew. Chem. Int. Ed.* **2015**, *54*, 2100–2104.

[34] Ferrari, A. C. Raman spectroscopy of graphene and graphite: Disorder, electron–phonon coupling, doping and nonadiabatic effects. *Solid State Commun.* **2007**, *143*, 47-57.

[35] Hadjiev, V. G.; Iliev, M. N.; Vergilov, I. V. The Raman spectra of Co_3O_4. *J. Phys. C: Sol. State Phys.* **1988**, *21*, L199-L201.

[36] Saxena, P.; Varshney, D. Effect of d-block element substitution on structural and dielectric properties on iron cobaltite. *J. All. Comp.* **2017**, *705*, 320-326.

[37] Biesinger, M. C.; Payne, B. P.; Grosvenor, A. P.; Lau, L. W. M.; Gerson, A. R.; Smart, R. S. C. Resolving surface chemical states in XPS analysis of first row transition metals, oxides and hydroxides: Cr, Mn, Fe, Co and Ni. *Appl. Surf. Sci.* **2011**, *257*, 2717-2730.

[38] Cullity, B. D.; Graham, C. D. *Introduction to Magnetic Materials*, John Wiley & Sons, Inc., Hoboken, NJ, USA, **2008**, vol. 21.

[39] Zhang, Y.; Zhu, Y.; Wang, K.; Li, D.; Wang, D.; Ding, F.; Meng, D.; Wang, X.; Choi, C.; Zhang, Z., Controlled synthesis of Co2C nanochains using cobalt laurate as precursor: Structure, growth mechanism and magnetic properties. *Journal of Magnetism and Magnetic Materials* **2018,** *456*, 71-77.

[40] Desvaux, C.; Amiens, C.; Fejes, P.; Renaud, P.; Respaud, M.; Lecante, P.; Snoeck, E.; Chaudret, B., Multimillimetre-large superlattices of air-stable iron–cobalt nanoparticles. *Nature Mat.* **2005,** *4*, 750-753.

[41] Desvaux, C.; Dumestre, F.; Amiens, C.; Respaud, M.; Lecante, P.; Snoeck, E.; Fejes, P.; Renaud, P.; Chaudret, B., FeCo nanoparticles from an organometallic approach: synthesis, organisation and physical properties. *J. Mat. Chem.* **2009,** *19*, 3268-3275.

[42] Nogués, J.; Schuller, I. K. Exchange bias. *J. Magnet. Mag. Mat.* **1999**, *192*, 203-232.

[43] Saville, S. L.; Qi, B.; Baker, J.; Stone, R.; Camley, R. E.; Livesey, K. L.; Ye, L.; Crawford, T. M.; Thompson Mefford, O. The formation of linear aggregates in magnetic hyperthermia: Implications on specific absorption rate and magnetic anisotropy. *J. Colloid Interf. Sci.*, **2014**, *424*, 141–151.

[44] Mehdaoui, B.; Tan, R. P.; Meffre, A.; Carrey, J.; Lachaize, S.; Chaudret, B.; Respaud, M. Increase of magnetic hyperthermia efficiency due to dipolar interactions in low-anisotropy magnetic nanoparticles: Theoretical and experimental results. *Phys. Rev. B - Condens. Matter Mater. Phys.* **2013**, *87*, 1–10.

[45] Mehdaoui, B.; Meffre, A.; Lacroix, L. M.; Carrey, J.; Lachaize, S.; Gougeon, M.; Respaud, M.; Chaudret, B. Magnetic anisotropy determinartion and magnetic hyperthermia properties of small Fe nanoparticles in the superparamagnetic regime. *J. Appl. Phys.* **2010**, *107*, 09A324.

[46] Serantes, D.; Simeonidis, K.; Angelakeris, M.; Chubykalo-Fesenko, O.; Marciello, M.; Morales, M. d. P.; Baldomir, D.; Martinez-Boubeta, C. Multiplying Magnetic Hyperthermia Response by Nanoparticle Assembling. *J. Phys. Chem. C*, **2014**, *118*, 5927–5934.

[47] Asensio, J. M.; Marbaix, J.; Mille, N.; Lacroix, L.-M.; Soulantica, K.; Fazzini, P.-F.; Carrey, J.; Chaudret, B. To heat or not to heat: a study of the performances of iron carbide nanoparticles in magnetic heating. *Nanoscale* **2019**, *11*, 5402-5411.

[48] A control experiment was carried out to take into account the temperature deviations due to the eddy currents at the thermocouple during the catalysis. Therefore, temperatures given are an estimation which were validated by IR camera

[49] Xiong, H.; Lin, S.; Goetze, J.; Pletcher, P.; Guo, H.; Kovarik, L.; Artyushkova, K.; Weckhuysen, B. M.; Datye, A. K. Thermally Stable and Regenerable Platinum–Tin Clusters for Propane Dehydrogenation Prepared by Atom Trapping on Ceria. *Angew. Chem. Int. Ed.* **2017**, *56*, 8986-8991.

[50] Zhu, Y.; An, Z.; Song, H.; Xiang, X.; Yan, W.; He, J. Lattice-Confined Sn (IV/II) Stabilizing Raft-Like Pt Clusters: High Selectivity and Durability in Propane Dehydrogenation. *ACS Catal.* **2017**, *7*, 6973-6978.

[51] Hauser, A. W.; Gomes, J.; Bajdich, M.; Head-Gordon, M.; Bell, A. T. Subnanometer-sized Pt/Sn alloy cluster catalysts for the dehydrogenation of linear alkanes. *Phys. Chem. Chem. Phys.* **2013**, *15*, 20727-20734.

[52] Lee, M.-H.; Nagaraja, B. M.; Lee, K. Y.; Jung, K.-D. Dehydrogenation of alkane to light olefin over PtSn/θ-Al$_2$O$_3$ catalyst: Effects of Sn loading. *Catal. Today*, **2014**, *232*, 53–62.

[53] Bursavich, J.; Abu-Laban, M.; Muley, P. D.; Boldor, D.; Hayes, D. J., Thermal performance and surface analysis of steel-supported platinum nanoparticles designed for bio-oil catalytic

upconversion during radio frequency-based inductive heating. *Energ. Convers. Manage.* **2019,** *183*, 689-697.

[54] Pashchenko, D. Thermodynamic equilibrium analysis of combined dry and steam reforming of propane for thermochemical waste-heat recuperation. *Int. J. Hydrogen Energ.* **2017,** *42,* 14926-14935.

[55] Ojeda, M.; Nabar, R.; Nilekar, A. U.; Ishikawa, A.; Mavrikakis, M.; Iglesia, E. CO activation pathways and the mechanism of Fischer–Tropsch synthesis. *J. Catal.*, **2010**, *272*, 287–297.

[56] Gao, J.; Wang, Y.; Ping, Y.; Hu, D.; Xu, G.; Gu, F.; Su, F. A thermodynamic analysis of methanation reactions of carbon oxides for the production of synthetic natural gas. *RSC Adv.* **2012**, *2*, 2358-2368.

[57] Zangeneh, F. T.; Taeb, A.; Gholivand, K.; Sahebdelfar, S. Thermodynamic Equilibrium Analysis of Propane Dehydrogenation with Carbon Dioxide and Side Reactions. *Chem. Eng. Commun.* **2016**, *203*, 557-565.

[58] Wang, X.; Wang, N.; Zhao, J.; Wang, L. Thermodynamic analysis of propane dry and steam reforming for synthesis gas or hydrogen production. *Int. J. Hydrogen Energ.* **2010**, *35*, 12800-12807.

[59] Martínez-Prieto, L. M.; Puche, M.; Cerezo-Navarrete, C.; Chaudret, B. Uniform Ru nanoparticles on N-doped graphene for selective hydrogenation of fatty acids to alcohols. *J. Catal.* **2019**, *377*, 429-437.

[60] Soulantica, K.; Maisonnat, A.; Fromen, M.-C.; Casanove, M.-J.; Chaudret, B. Spontaneous Formation of Ordered 3D Superlattices of Nanocrystals from Polydisperse Colloidal Solutions. *Angew. Chem. Int. Ed.* **2003**, *42*, 1945-1949.